

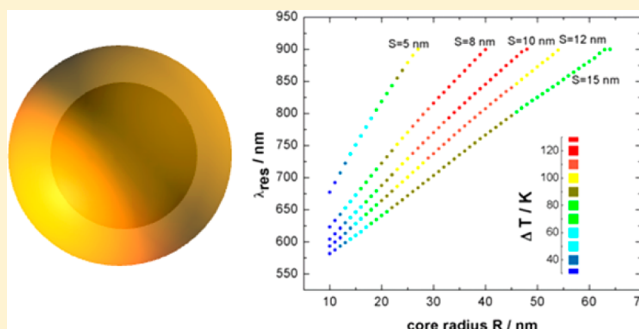
Size Optimization of Iron Oxide@Noble Metal Core–Shell Nanohybrids for Photothermal Applications

Ezequiel R. Encina and Eduardo A. Coronado*

INFIQC–CONICET, Departamento de Fisicoquímica, Facultad de Ciencias Químicas, Universidad Nacional de Córdoba, Córdoba 5000, Argentina

Supporting Information

ABSTRACT: The optical properties of several iron oxide@noble metal core–shell nanohybrids (NHs) have been systematically studied by means of electrodynamics simulations applying Mie theory for coated spheres. Focus has been made in analyzing the dependence of the absorption cross section C_{abs} on the composition as well as on the variables that determine the NHs size, that is, the core radius, R , and the shell thickness, S . The absorption spectra are characterized by an intense peak attributed to a plasmon resonance mode for which the spectral position can be finely tuned in the Vis–NIR range according to the NH size and composition. The absorption cross-section peak intensity, $C_{\text{abs,max}}$, a key quantity regarding photothermal applications, also presents a strong dependence on the NH size and composition. In general, it is found that $\alpha\text{-Fe}_2\text{O}_3\text{@Au}$ and $\alpha\text{-Fe}_2\text{O}_3\text{@Ag}$ lead to larger $C_{\text{abs,max}}$ values than $\text{Fe}_3\text{O}_4\text{@Au}$ and $\text{Fe}_3\text{O}_4\text{@Ag}$ core–shell NHs, which is attributed to the lower imaginary refractive index of $\alpha\text{-Fe}_2\text{O}_3$ in comparison to that of Fe_3O_4 . The theoretical $C_{\text{abs,max}}$ values were then used to calculate the temperature change ΔT experienced by the NH when its plasmon resonance mode is excited on resonance. This information has been summarized in diagrams that relate, for each NH composition, the core radius R , the shell thickness S , its resonance wavelength, and the temperature change ΔT experienced at their resonance wavelength. This set of diagrams summarizes relevant information that allows us to predict, for instance, the size and composition that a NH should have to produce the largest ΔT upon illumination at a certain wavelength. The results presented in this work should be helpful to guide and optimize the design of magnetic-plasmonic core–shell NHs with potential photothermal applications.



INTRODUCTION

Nanostructured materials of different nature have been intensively investigated during the past decade mainly because of their size- and shape-dependent physical and chemical properties, showing great potential in several fields such as solar energy conversion, catalysis, and biomedicine.^{1–7} With regard to noble metal nanoparticles, their outstanding optical properties are characterized by size- and shape-tunable localized surface plasmon resonances that give rise to large absorption and scattering cross sections.^{8,9} This point illustrates the importance of the close structure–function relationship exploited in nanotechnology. For example, relatively large size noble metal nanoparticles would be more appropriate for devices that require large amounts of scattered light; on the contrary, rather small nanoparticles would be more efficient in cases when light absorption is demanded.¹⁰ In addition, part of the absorbed electromagnetic energy is transformed into heat via relaxation processes, and several experimental and theoretical studies have been performed to determine the temperature increase in the local environment of the illuminated nanostructures.^{11–18} Magnetite (Fe_3O_4) and hematite ($\alpha\text{-Fe}_2\text{O}_3$) are the most thermodynamically stable polymorphs of iron oxides, and its nanoparticulated materials present a great scientific and

technological interest.¹⁹ Magnetite nanoparticles are recognized for their ferrimagnetic properties, which are exploited, for instance, in biomedicine and catalysis.^{20,21} The weakly ferromagnetic hematite phase presents n-type semiconductor behavior, which is exploited in sunlight-driven water-splitting photoelectrochemical cells, to name just a few applications.^{22,23} Recently, Manukyan et al. reported the synthesis of ultrasmall $\alpha\text{-Fe}_2\text{O}_3$ superparamagnetic nanoparticles with unusually high magnetization.²⁴

Nonetheless, when these two different types of materials are brought together into multifunctional structures, possibilities for a new number of applications arise.^{25–27} The core–shell geometry is likely the most common found among the several chemically prepared NHs, whereas the different ways to arrange the composition and size of the core and shell lead to a relatively large number of NHs with distinct identity and properties.^{28–32} In particular, Au, a plasmonic active metal, together with Fe_3O_4 and $\alpha\text{-Fe}_2\text{O}_3$ iron oxides has been largely employed to synthesize core–shell NHs mainly due to their multifunction features.^{33–40}

Received: November 10, 2015

Revised: February 16, 2016

Published: February 18, 2016



The incorporation of iron oxide nanoparticles into more complex nanostructures allowed the development of magnetically recyclable catalyst and biocompatible nanoparticles for use as magnetic drug-targeting agents, as magnetic resonance imaging (MRI) contrast agents, and for protein separation.^{41–46} On the other hand, dielectric core–noble metal shell NHs present plasmon resonances having resonance wavelengths typically within the NIR region of the spectrum.^{47–49} Given that human tissue exhibits a high transmittance of electromagnetic radiation in the NIR region, it has been purposed for the use of iron oxide core–noble metal shell NHs with magnetic-plasmonic properties for photothermal applications.^{50–52}

In particular, for photothermal applications, maximizing the absorption of electromagnetic radiation in the NIR region by means of the geometric parameters of the NHs is a relevant issue to improve their performance.⁵³ However, to the best of our knowledge, there still exists a need to investigate the size and composition of the core and shell that give rise to the highest absorption cross section within the NIR region of the spectrum and consequently to the larger temperature change ΔT . From the experimental point of view, it seems to be not simple to address this point. Besides the difficulties associated with the precise control of the NH dimensions over a relatively broad range, standard techniques, such as UV–visible spectroscopy, provide extinction rather than absorption measurements because scattering processes become more important as the total size of the nanostructure increases. In this respect, the computational design could be very helpful; particularly electrodynamics simulations can be employed to accurately calculate both absorption and scattering spectra and in this way determine the dependence of the absorption cross sections on the composition and size of core–shell NHs. Although there are a number of previous works in which the extinction, absorption, and scattering cross sections of Fe_3O_4 @Au core–shell NHs have been simulated using the extended Mie theory to multilayered spherical structures, they have not been focused in analyzing their performance as optical heat sources.^{54,55} An investigation more related to the present work was reported by Li et al., in which the photothermal properties of three kinds of Au– SiO_2 core–shell NHs have been studied through simulations based on commercially available finite element method solver.⁵⁶

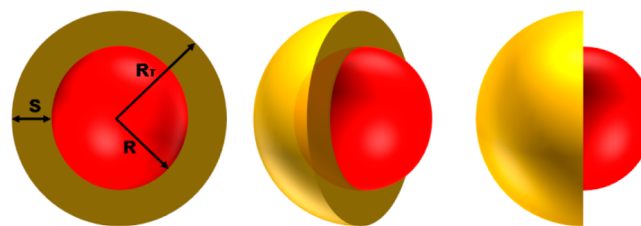
In this work, the optical properties of Fe_3O_4 @Au, Fe_3O_4 @Ag, $\alpha\text{-Fe}_2\text{O}_3$ @Au, and $\alpha\text{-Fe}_2\text{O}_3$ @Ag core–shell NHs have been systematically simulated by applying Mie theory for coated spheres. Special emphasis has been made in analyzing the relationship between the absorption cross section, C_{abs} , and the NH composition as well as the variables that determine their size, that is, the core radius R and the shell thickness S . In general, it has been found that $\alpha\text{-Fe}_2\text{O}_3$ @Au and $\alpha\text{-Fe}_2\text{O}_3$ @Ag present larger $C_{\text{abs,max}}$ values than Fe_3O_4 @Au and Fe_3O_4 @Ag core–shell NHs due to the intrinsic dielectric properties of the core material. The theoretical $C_{\text{abs,max}}$ values were then used to calculate the temperature change ΔT experienced by the NH when its plasmon resonance mode is excited on resonance. This information has been summarized in diagrams that relate, for each NH composition, the core radius R , the shell thickness S , its resonance wavelength, and the temperature change ΔT experienced at their resonance wavelength. Therefore, this set of diagrams allows us to predict, for instance, the size that a given type of NH should have to produce the largest ΔT upon illumination at a certain wavelength. We believe these results should help to guide the significant experimental efforts toward

the optimum design of magnetic-plasmonic core–shell NHs for photothermal applications.

THEORETICAL METHODS

The Mie theory for coated spheres, which constitutes an exact solution to the problem of absorption and scattering of light by an object composed by concentric spheres, was employed to simulate the optical properties of core–shell NHs. A complete and detailed description of this method can be found in the book written by Bohren and Hoffman.⁵⁷ In particular, this theoretical methodology was used to simulate the extinction, scattering, and absorption cross sections of Fe_3O_4 @Au, $\alpha\text{-Fe}_2\text{O}_3$ @Au, Fe_3O_4 @Ag, and $\alpha\text{-Fe}_2\text{O}_3$ @Ag core–shell NHs. The wavelength-dependent complex refractive indices for Au and Ag were obtained from ref 58, whereas the corresponding data for Fe_3O_4 and $\alpha\text{-Fe}_2\text{O}_3$ were obtained from refs 59 and 60, respectively. The calculations were performed using water ($n = 1.33$) as the dielectric surrounding media. The core radius, R , was varied systematically between 10 and 100 nm, whereas the shell thickness, S , was varied between 1 and 15 nm (see Scheme 1) to study their influence on the optical response, especially on the absorption cross section, C_{abs} . All of the simulations were performed using the BHCOAT code.

Scheme 1. Different Schematic Views of the Model Used To Represent the Iron Oxide@Noble Metal Core–Shell NHs in the Mie Theory for Coated Spheres Calculations^a



^a S , shell thickness; R , core radius; R_T , total NH radius (indicated in the left panel).

RESULTS AND DISCUSSION

General Features of the Extinction Spectra of NHs. Let us first analyze the distinct contributions to the extinction spectra for particular NHs. Figure 1 shows extinction (C_{ext}), scattering (C_{sca}), and absorption cross section (C_{abs}) spectra of two different sizes of Fe_3O_4 @Au NHs dispersed in water. Each of these spectra is characterized by a well-defined peak having a spectral position that clearly depends on the NH size. To explain the optical properties of core (dielectric)–shell (metallic) nanostructures, Prodan et al. proposed a hybridization model, in which surface plasmons are formed at the inner shell–core interface (cavity) and on the outer metal surface (sphere).^{61,62} In turn, the cavity and sphere modes hybridize to form a red-shifted (lower energy) coupled plasmon mode and a blue-shifted (higher energy) anticoupled plasmon mode. Thus, according to the hybridization model, the peaks at 670 nm (black solid line curve) and 776 nm (black dashed line curve) in the extinction spectra of the $R = 25$ nm– $S = 15$ nm and $R = 40$ nm– $S = 10$ nm NH, respectively, can be associated with the above-mentioned coupled plasmon modes. In these cases, the anticoupled mode is not observed in the spectra, although it can be observed in cases when the imaginary component of the core refractive index is significantly large.

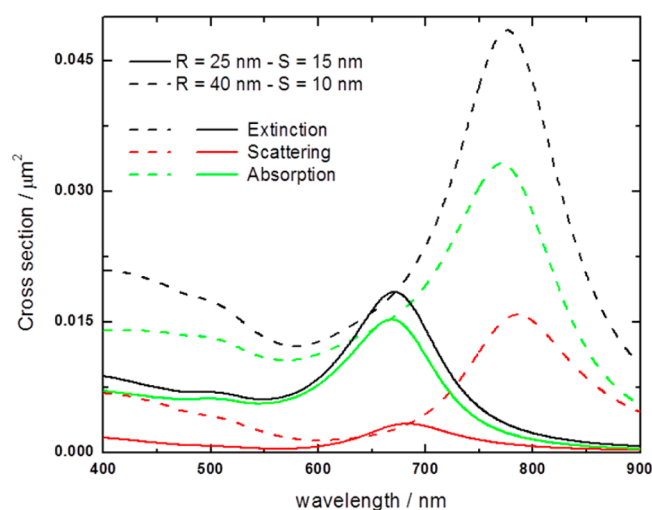


Figure 1. Extinction, scattering, and absorption cross-section spectra of two different sizes of $\text{Fe}_3\text{O}_4@Au$ NHs dispersed in water.

Jain and El-Sayed have shown that, for silica or hollow cores, the magnitude of the red-shift of the coupled mode increases as

the ratio of Au shell thickness to core radius decreases.⁶³ More specifically, these authors fitted the red-shift of the coupled mode to the universal scaling equation

$$\frac{\Delta\lambda_{\text{res}}}{\lambda_0} = A \exp\left(\frac{(-S/R)}{B}\right) \quad (1)$$

where λ_0 corresponds to the plasmon resonance wavelength of a solid Au sphere of radius $R + S$, λ_{res} corresponds to the resonance wavelength of the coupled mode of the core-shell nanostructure, $\Delta\lambda_{\text{res}} = \lambda_{\text{res}} - \lambda_0$, and A and B are constants. More recently, Chaffin et al. have determined a similar scaling relationship between $\lambda_{\text{res}}/\lambda_0$ and S/R for $\text{Fe}_3\text{O}_4@Au$ NHs, where $A = 0.73$ and $B = 0.39$.⁵⁵ Note that eq 1 qualitatively describes the changes observed in the extinction spectra shown in Figure 1, given that the spectrum of the NH with the smaller S/R ratio exhibits the larger red-shift. Furthermore, the other NH compositions investigated show also the same trends (see Figure S1 in the Supporting Information (SI)). Even though the relatively simple scaling relationship in eq 1 provides valuable information, particularly, the spectral position of the plasmon coupled mode for a given NH, our interest is to know the resonance values of the absorption and scattering cross sections at the resonance

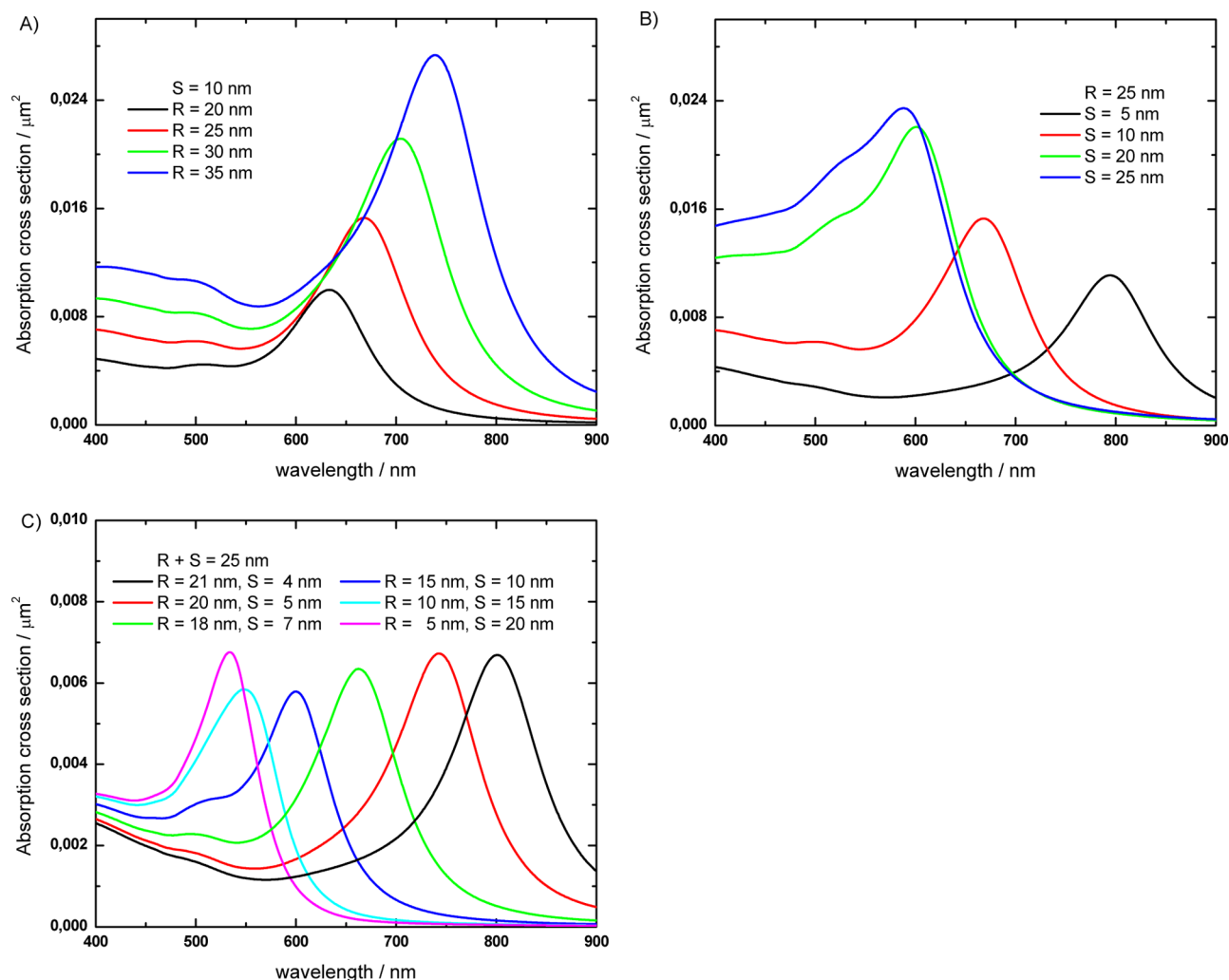


Figure 2. Effects of core radius R and shell thickness S on the absorption C_{abs} spectra of $\text{Fe}_3\text{O}_4@Au$ NHs dispersed in water: (A) effect of varying R , keeping S constant at 10 nm; (B) effect of varying S , keeping R constant at 25 nm; (C) effect of varying R and S , keeping the total radius $R_T (= R + S)$ constant at 25 nm.

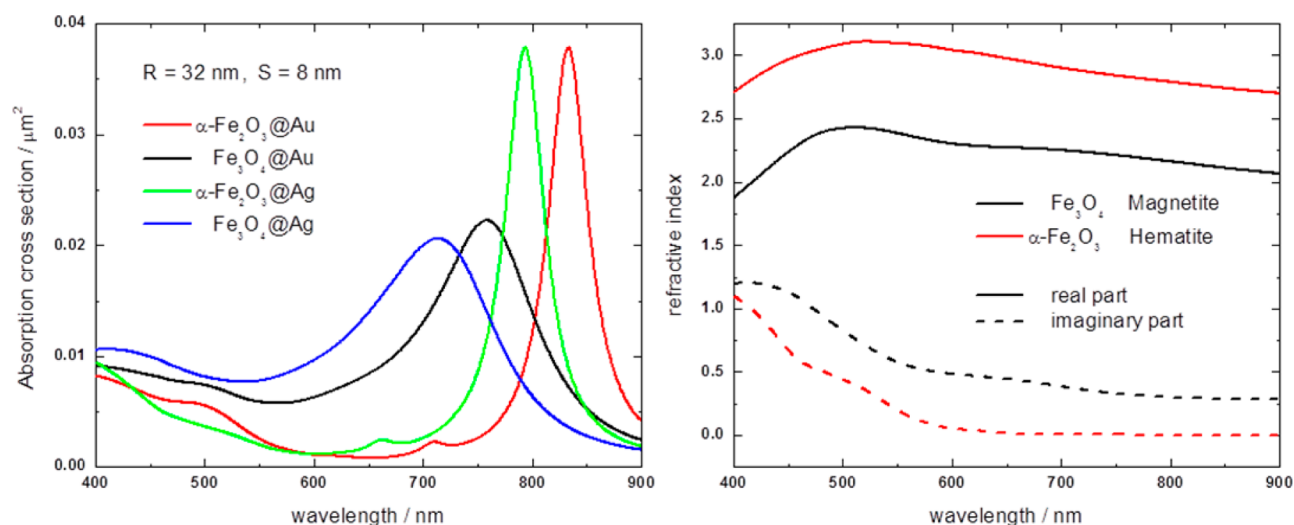


Figure 3. (A) Absorption spectra of NHs all with the same size ($R = 32$ nm and $S = 8$ nm) and with different core and shell compositions. (B) Real and imaginary parts of the wavelength-dependent refractive indices for magnetite (Fe_3O_4) and hematite ($\alpha\text{-Fe}_2\text{O}_3$). Magnetite and hematite refractive index values were obtained from refs 59 and 60, respectively.

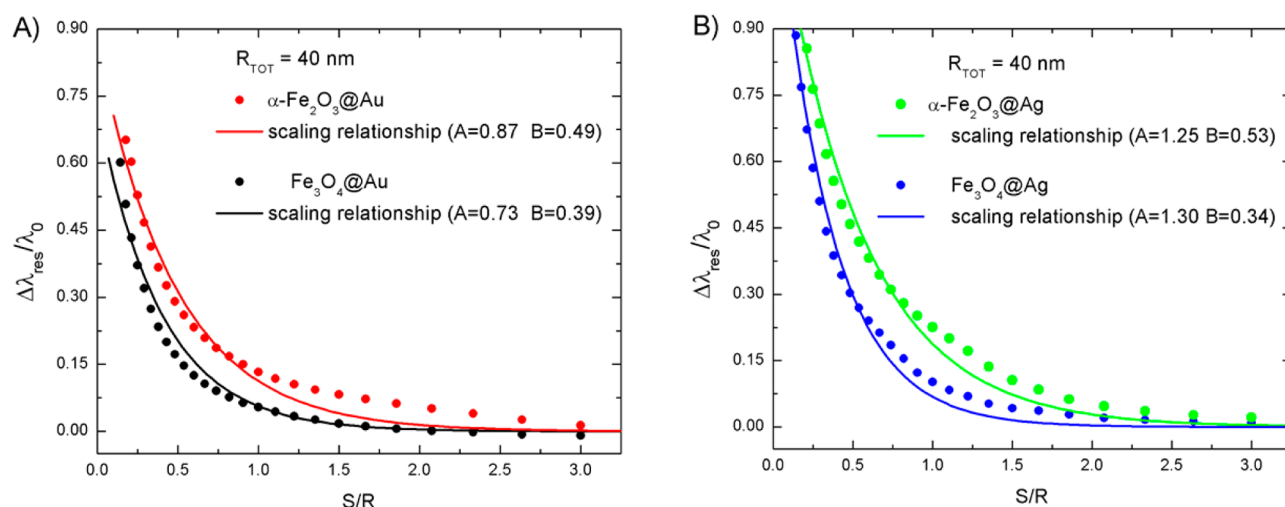


Figure 4. Fractional shift $\Delta\lambda_{\text{res}}/\lambda_0$ for NHs of different core and shell compositions: (A) data for $\alpha\text{-Fe}_2\text{O}_3\text{@Au}$ and $\text{Fe}_3\text{O}_4\text{@Au}$ NHs (dots); (B) data for $\alpha\text{-Fe}_2\text{O}_3\text{@Ag}$ and $\text{Fe}_3\text{O}_4\text{@Ag}$ NHs (dots). The total radius $R_T (= R + S)$ is 40 nm in all cases. The solid curves in both panels represent the scaling relationship eq 1 with the respective A and B values for each NH composition as indicated in the legend.

wavelength. With regard to specially the potential photothermal applications of this kind of nanostructures, the absorption cross section C_{abs} is a quantity of paramount importance given that it determines to great extent the efficiency of the process of conversion of light into heat. As far as we know, scaling relationships that estimate the absolute C_{abs} or its relative contributions to extinction as a function of NH size have not been reported; therefore, this estimation has to be performed individually for each particular nanostructure. It is also important to note that, as a consequence of the scattering process, absorption cross sections or efficiencies are not easily accessible through simple experimental techniques such as UV–vis spectroscopies, which generally provide extinction measurements. Thus, as our main goal is to analyze their applications in photothermal devices, in the following we will focus on investigating mainly their absorption properties.

Effects of Core Radius and Shell Thickness on C_{abs}

Figure 2 shows different sets of representative calculations to exemplify the effect of core radius R and shell thickness S on the

absorption spectra for $\text{Fe}_3\text{O}_4\text{@Au}$ NHs dispersed in water. It is easily appreciable that by increasing the core radius R from 20 to 35 nm, at a constant shell thickness $S = 10$ nm (Figure 2A), a significant red-shift of the resonance wavelength of the plasmon coupled mode, λ_{res} , is produced. As mentioned above, $C_{\text{abs,max}}$, that is, the C_{abs} value at λ_{res} , constitutes the relevant quantity for the purposes of this work because it greatly determines the amount of light energy that can be converted into heat by a given NH. From the set of spectra shown in Figure 2A, it can be observed that the larger λ_{res} , the higher the $C_{\text{abs,max}}$. Alternatively, increasing S from 5 to 25 nm, keeping R constant at a value of 25 nm (Figure 2B), leads to a noticeable blue-shift of λ_{res} . Note that, in this case, $C_{\text{abs,max}}$ decreases as λ_{res} shifts approximately from 550 nm to almost 800 nm. It is also instructive to analyze the behavior of λ_{res} and $C_{\text{abs,max}}$ when R and S are modified simultaneously, keeping the total size of the NH ($R+S$) at a constant value of 25 nm (Figure 2C). In this case, the same trend found in the previous examples is observed, that is, λ_{res} red-shifts as the ratio S/R decreases. However, the $C_{\text{abs,max}}$ values do not

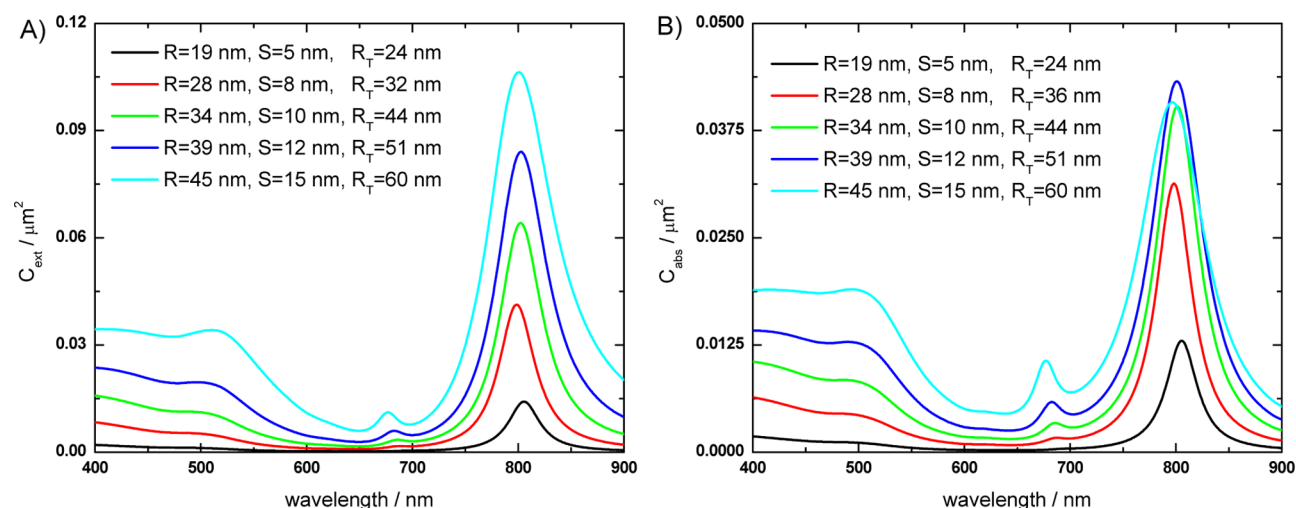


Figure 5. (A) C_{ext} and (B) C_{abs} spectra of $\alpha\text{-Fe}_2\text{O}_3\text{@Au}$ NHs of different core radii R and shell thicknesses S as indicated in the legends. The R and S values have been selected in such a way that $\lambda_{\text{res}} \approx 800$ nm.

change significantly with λ_{res} , particularly for λ_{res} values lying in the NIR region of the spectrum. In general, the results presented in Figure 2 clearly show that it is possible to tune the λ_{res} value from the visible to the NIR region of the electromagnetic spectrum by selecting the appropriate values for the core radius R and shell thickness S .

More specifically, it is found, in agreement with previous results,⁶³ that the smaller the S/R ratio, the larger the λ_{res} red-shift. On the other hand, it is also observed that the variation of the $C_{\text{abs,max}}$ values does not exhibit a clear trend with the associated λ_{res} values. The same qualitative behavior has been found for the other NH compositions studied in this work (see Figures S2–S4, SI). Therefore, to find the largest $C_{\text{abs,max}}$ value, it seems to be necessary to analyze in a more systematic way its variation for a wide range of R and S values.

Effects of Core and Shell Composition on C_{abs} . To illustrate the effects of the nature of both the dielectric core and the metallic shell, Figure 3A shows absorption spectra of NHs with different core and shell compositions ($\alpha\text{-Fe}_2\text{O}_3\text{@Au}$, $\text{Fe}_3\text{O}_4\text{@Au}$, $\alpha\text{-Fe}_2\text{O}_3\text{@Ag}$, and $\text{Fe}_3\text{O}_4\text{@Ag}$), all with the same size $R = 32$ nm and $S = 8$ nm. For NHs with the same dielectric core, the Au shell leads to a plasmon resonance at larger wavelength than the Ag shell, whereas the $C_{\text{abs,max}}$ values are quite similar. On the other hand, the change from Fe_3O_4 to $\alpha\text{-Fe}_2\text{O}_3$, keeping the same metallic shell, give place to a red-shift of λ_{res} as well as to a significant increase of $C_{\text{abs,max}}$. Importantly, these results are in agreement with previous studies.⁵⁵ These different optical responses can be interpreted in terms of the hybridization model and the respective complex refractive indices of the core materials constituting the NHs (see Figure 3B).

The larger real refractive index of $\alpha\text{-Fe}_2\text{O}_3$ in comparison with Fe_3O_4 generates a lower frequency cavity plasmon, resulting in a larger red-shift, that is, a larger λ_{res} value. In turn, the lower imaginary refractive index of $\alpha\text{-Fe}_2\text{O}_3$ in comparison with Fe_3O_4 suggests an increase in the coupling between the cavity and sphere plasmon modes, leading to an increase in the intensity of the absorption peak. As will be shown below, the differences in the $C_{\text{abs,max}}$ value achieved by each NH has an important impact regarding its potential photothermal applications. The effect of the dielectric core nature is further exemplified in Figure 4, where the dependence of the fractional red-shift, $\lambda_{\text{res}}/\lambda_0$, on the S/R ratio for core–shell NHs with constant total radius $R_T (= R + S)$ of 40

nm is shown. It is observed that, for each particular NH composition, the $\Delta\lambda_{\text{res}}/\lambda_0$ values follow the same trend, decaying exponentially to zero as the S/R ratio $\rightarrow \infty$, that is, as the NH composition approaches a homogeneous metallic sphere. The qualitatively similar behavior shown in Figure 4 indicates that such dependence is mainly due to the NH geometry, whereas the quantitative differences between the specific $\Delta\lambda_{\text{res}}/\lambda_0$ values are attributed to differences in the respective refractive indices as mentioned above. Note that the scaling relationship reported by Chaffin et al.⁵⁵ has also been plotted in Figure 4A (solid black curve) for reference. The scaling law, as expected, fits the $\text{Fe}_3\text{O}_4\text{@Au}$ NHs data, and the small deviations observed can be attributed to retardation effects (Figure 4A).

However, as all of the different NH compositions follow an exponential decay, eq 1 could still be employed to quantitatively fit the data by determining the corresponding A and B values. In fact, the data for the other NH compositions have also been fitted using eq 1 (see Figure 4, solid curves), whereas the A and B values for each composition are indicated in the legend of Figure 4. Interestingly, the A parameter value seems to have a more noticeable dependence on the shell material nature, whereas, in contrast, the B value shows a more pronounced dependence on the core material composition. The results presented to this point clearly show that it is possible to accurately estimate λ_{res} by means of a scaling relationship of the type of eq 1 as well as that it can be tuned in the whole vis–NIR range by changing the R and S values.

With regard to photothermal applications, $C_{\text{abs,max}}$ is the key quantity; nonetheless, there does not seem to be a simple and direct way to estimate it from λ_{res} , R , and S values. This aspect is exemplified in Figure 5, where C_{ext} and C_{abs} spectra of different sizes of $\alpha\text{-Fe}_2\text{O}_3\text{@Au}$ NHs are shown in panels A and B, respectively.

The R and S values have been selected in such a way that $\lambda_{\text{res}} \approx 800$ nm. On the one hand, it can be clearly appreciated that the extinction peak intensity is proportional to the NH total radius $R_T (= R + S)$, which is due to a larger scattering contribution and to the larger volume of gold in the shell (Figure 5a). However, it is rather hard to determine from these extinction spectra which of the different sizes of NHs presents the highest $C_{\text{abs,max}}$ value. On the other hand, simulated absorption spectra show that $C_{\text{abs,max}}$ first increases and then decreases as the NH total radius R_T is

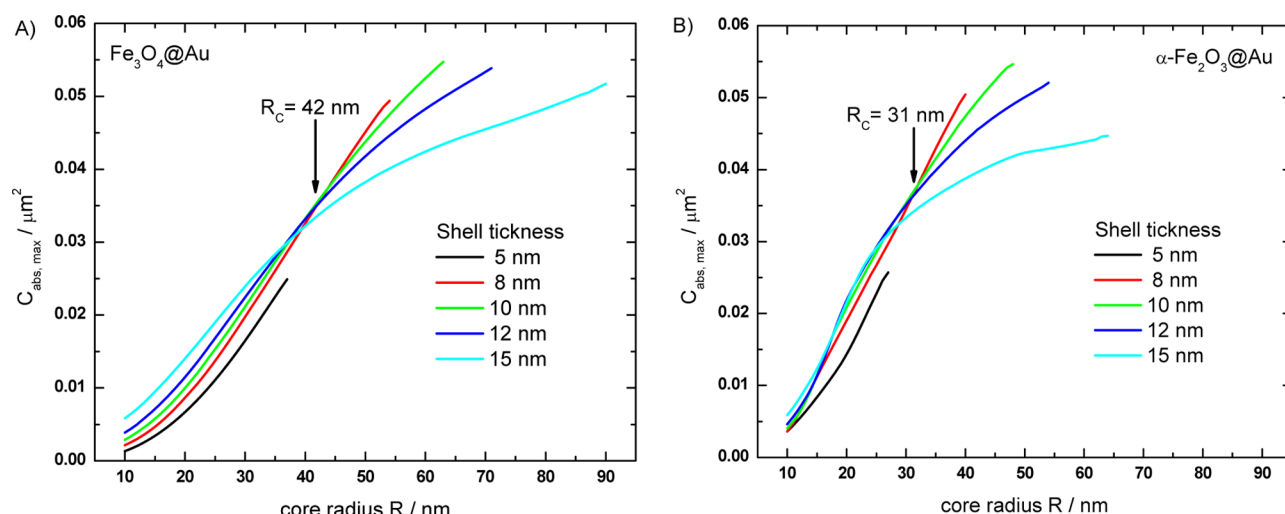


Figure 6. Variation of $C_{\text{abs,max}}$, that is, C_{abs} evaluated at λ_{res} , with the core radius R for different shell thickness S values. Data correspond to (A) $\text{Fe}_3\text{O}_4@Au$ and (B) $\alpha\text{-Fe}_2\text{O}_3@Au$ NHs.

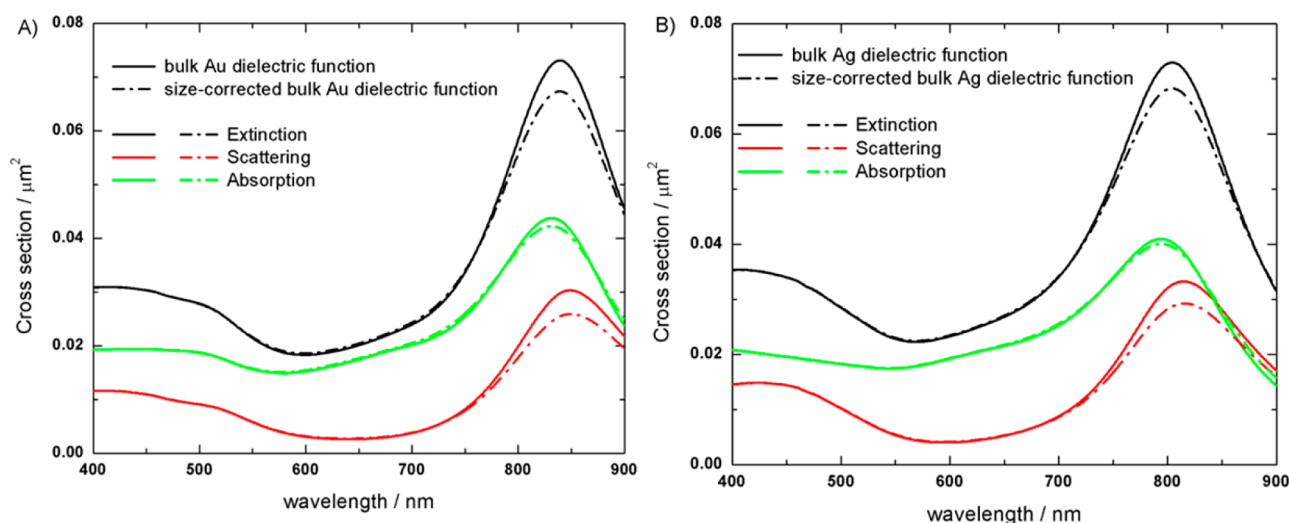


Figure 7. Extinction, scattering, and absorption cross-section spectra of (A) $Au@Fe_3O_4$ and (B) $Ag@Fe_3O_4$ NHs. In both cases $R = 50$ nm and $S = 10$ nm. Solid and dash-dot curves correspond to spectra simulated with the bulk and size-corrected dielectric function of the metallic shell material, respectively.

increased, showing that there is not a direct proportionality between $C_{\text{abs,max}}$ and R_T .

Figure 6 shows the variation of $C_{\text{abs,max}}$ with the core radius R for different shell thickness S values for (A) $\text{Fe}_3\text{O}_4@Au$ and (B) $\alpha\text{-Fe}_2\text{O}_3@Au$ NHs. It is important to note that as R increases, for a constant S value, λ_{res} concomitantly increases. Thus, the respective λ_{res} values for the $C_{\text{abs,max}}$ data plotted in Figure 6 lie in the range $\lambda_0 \leq \lambda_{\text{res}} \leq 900$ nm, the upper calculated value being determined by the available complex refractive indexes experimental data (Figure 3B).

In general, it is found that, for a given S value, $C_{\text{abs,max}}$ exhibits a sigmoidal dependence on R . The same general trend has been found for $\text{Fe}_3\text{O}_4@Ag$ and $\alpha\text{-Fe}_2\text{O}_3@Ag$ NHs (see Figure S5, SI). In addition, for each specific NH composition, the different curves seem to cross each other at a common R value (R_C), where two different regimes can be identified through the comparison of R with R_C . Note that, as indicated by the arrows in Figure 6, $R_C = 42$ nm for $\text{Fe}_3\text{O}_4@Au$, whereas $R_C = 31$ nm for $\alpha\text{-Fe}_2\text{O}_3@Au$ NHs. Therefore, for $R < R_C$, $C_{\text{abs,max}}$ is proportional to R_T , and, for $R > R_C$, $C_{\text{abs,max}}$ decreases with R_T . This analysis indicates that

besides the relative contributions to extinction from absorption and scattering processes, the absolute $C_{\text{abs,max}}$ value first increases with R_T ; that is, with the total radius of the NH, up to a certain R_C value, and above it, $C_{\text{abs,max}}$ decreases as R_T further increases. Moreover, from the results presented in Figure 6, it is possible to find a set of R and S values that depend on the NH composition that produces the highest $C_{\text{abs,max}}$ value in the range $\lambda_0 \leq \lambda_{\text{res}} \leq 900$ nm. For the $\text{Fe}_3\text{O}_4@Au$ NHs case, these values are $R = 63$ nm and $S = 10$ nm, whereas for $\alpha\text{-Fe}_2\text{O}_3@Au$ NHs these values are $R = 48$ nm and $S = 10$ nm.

Size Correction Effects of the Metallic Shell Dielectric Constant. It is known that for particles with dimensions smaller than the mean free path of the conduction electrons, the dielectric constant ϵ has a size dependence. Therefore, the effects of size correction of the dielectric constant for the metallic shell on the simulated spectra were also investigated. Such a size correction was performed according to the expression⁶⁴

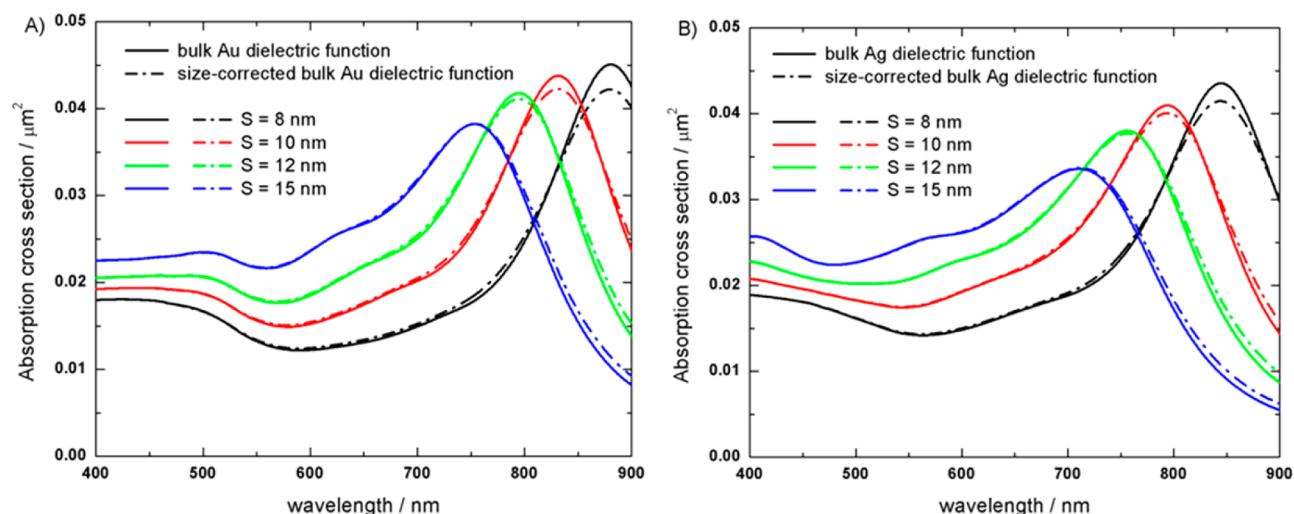


Figure 8. Absorption spectra of different shell thickness S and $R = 50$ nm for (A) $\text{Au}@\text{Fe}_3\text{O}_4$ and (B) $\text{Ag}@\text{Fe}_3\text{O}_4$ NHs. Solid and dash-dot curves correspond to spectra simulated with the bulk and size-corrected dielectric function of the metallic shell material, respectively.

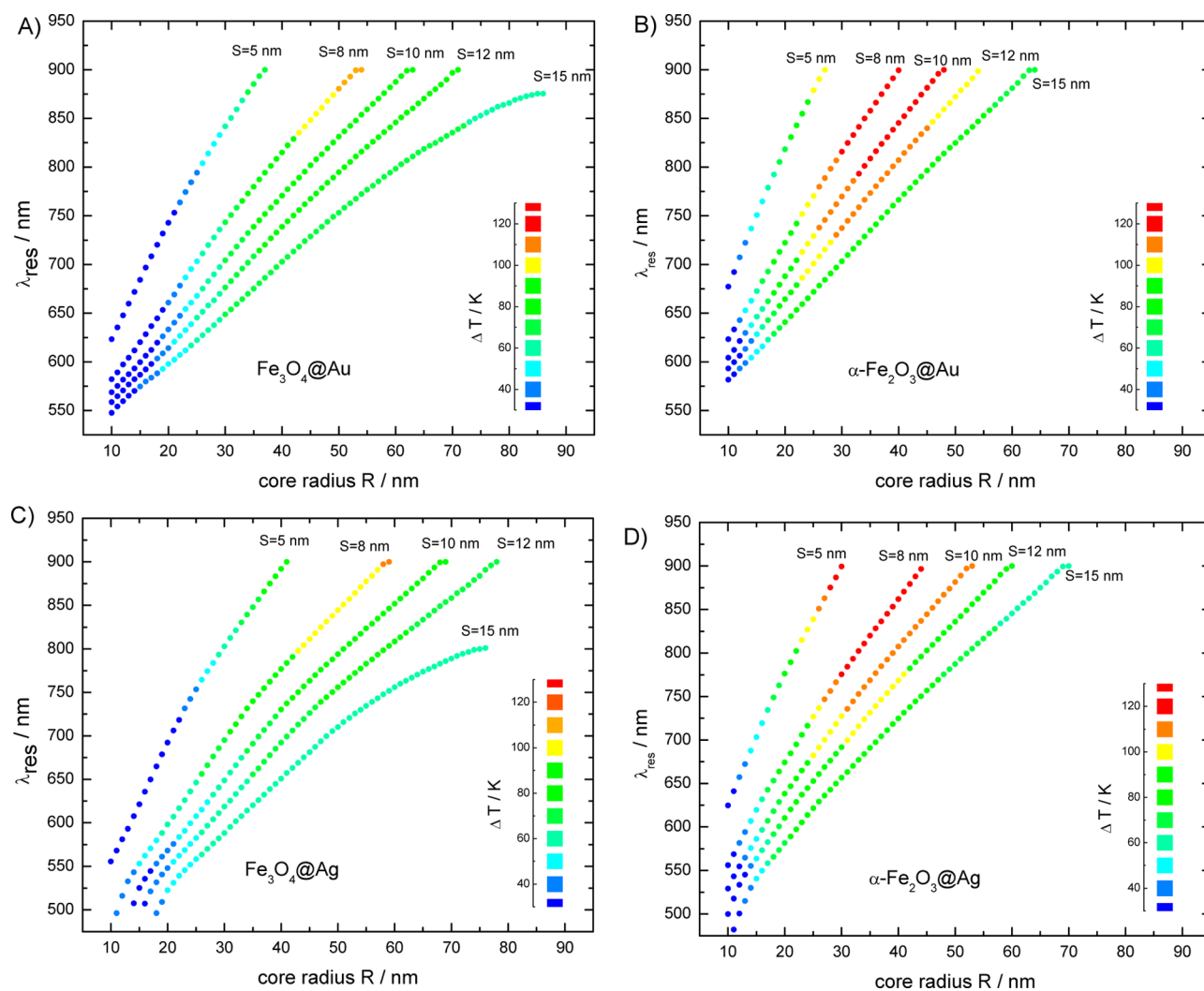


Figure 9. Variation of λ_{res} with the core radius R for different shell thickness S values. Data correspond to (A) $\text{Fe}_3\text{O}_4@\text{Au}$, (B) $\alpha\text{-Fe}_2\text{O}_3@\text{Au}$, (C) $\text{Fe}_3\text{O}_4@\text{Ag}$, and (D) $\alpha\text{-Fe}_2\text{O}_3@\text{Ag}$ NHs. The color code of the curves represents the ΔT values achieved at the surface of the NHs when they are dispersed in water and illuminated at their respective λ_{res} values with an irradiance of $1 \text{ mW } \mu\text{m}^{-2}$.

$$\varepsilon(\omega, L_{\text{eff}}) = \varepsilon_{\text{bulk}} + \frac{\omega_p^2}{\omega^2 + i\omega\gamma_0} - \frac{\omega_p^2}{\omega^2 + i\omega\left(\gamma_0 + A \frac{v_F}{L_{\text{eff}}}\right)} \quad (2)$$

where ω_p is the plasmon frequency and the constant γ_0 describes the intrinsic width of the dipole plasmon polariton. The term A is a dimensionless parameter, usually assumed to be close to unity, that is determined by details of the scattering process; v_F is the Fermi velocity, and L_{eff} is the effective mean free path of the conduction electrons. In turn, according to previous studies regarding spherical shell geometry, $L_{\text{eff}} = 4V/S$, where V and S are the volume and surface of the spherical shell, respectively.⁶⁵ The values of the different constants in eq 3, used to apply the size correction of the bulk dielectric constant $\varepsilon_{\text{bulk}}$ for Au and Ag, where $\omega_{p,\text{Au}} = \omega_{p,\text{Ag}} = 1.37 \times 10^{16} \text{ s}^{-1}$, $A_{\text{Au}} = A_{\text{Ag}} = 1$, $v_{F,\text{Au}} = v_{F,\text{Ag}} = 1.4 \times 10^6 \text{ ms}^{-1}$, $\gamma_{0,\text{Au}} = 1 \times 10^{14} \text{ s}^{-1}$, and $\gamma_{0,\text{Ag}} = 2.7 \times 10^{13} \text{ s}^{-1}$. It was found that, whatever the composition of the core and shell materials, the spectral position of the plasmon resonance does not change after the size correction of the metallic shell dielectric constant. On the other hand, it produces a decrease of the extinction peak intensity, increasing its full width at half-maximum. Moreover, it was also found that such a decrease in the extinction peak intensity is mainly due to a decrease in the scattering cross-section intensity, whereas the absorption cross-section intensity decreases but in a smaller proportion. These effects can be appreciated in the examples presented in Figure 7, where the respective extinction, scattering, and absorption spectra for (A) Au@Fe₃O₄ and (B) Ag@Fe₃O₄ are shown. In both cases $R = 40 \text{ nm}$ and $S = 10 \text{ nm}$.

Figure 8 shows the absorption spectra of different shell thickness and $R = 50 \text{ nm}$ for (A) Au@Fe₃O₄ and (B) Ag@Fe₃O₄ NHs. It can be observed that the absorption peak intensity values, that is, the $C_{\text{abs,max}}$ obtained considering the size correction are slightly smaller than the values obtained without the correction. Moreover, the decrease in $C_{\text{abs,max}}$ after consideration of the size correction, is more pronounced the thinner the shell thickness. However, in all cases analyzed, the variations in the $C_{\text{abs,max}}$ values are small enough and do not modify the relationships between the data presented in Figure 6 and Figure S5 (SI).

Temperature Increase under Illumination on Resonance Conditions. Figure 9 shows the dependence of λ_{res} on R for different S values and for several NH compositions. In general, it is observed that, for a fixed S , λ_{res} increases almost linearly with R , or as mentioned above, λ_{res} increases as the S/R ratio decreases. The $C_{\text{abs,max}}$ values obtained through extended Mie theory simulations for the different sizes and compositions of NHs (presented in Figure 6 and Figure S5, SI) can be used to calculate the temperature increase ΔT at the surface of the NHs when they are illuminated on resonance. This temperature increase can be calculated according to the steady-state solution of the heat equation for a spherical particle in a homogeneous medium using the equation⁶⁶

$$\Delta T = \frac{C_{\text{abs,max}} I}{4\pi\kappa R_T} \quad (3)$$

where I is the light power density illuminating the NH and κ the thermal conductivity of the surrounding medium. These ΔT values are shown for each NH size and for each wavelength in Figure 9. Note that each curve in Figure 9 is plotted following a color code that represents the ΔT values achieved at the surface of the NH when they are illuminated on resonance with an irradiance of $1 \text{ mW}\mu\text{m}^{-2}$ and dispersed in water ($\kappa_{\text{water}} = 0.6 \text{ W}$

$\text{m}^{-1} \text{ K}^{-1}$), where the inset in each respective figure indicates the ΔT scale.

With regard to Fe₃O₄@Au NHs (Figure 7a), the highest ΔT of 110 K is reached for a NH with $R = 53 \text{ nm}$ and $S = 8 \text{ nm}$ illuminated at a wavelength of 900 nm. Note that these dimensions are different from those of the NH that produces the largest $C_{\text{abs,max}}$ ($R = 63 \text{ nm}$, $S = 10 \text{ nm}$). This effect is due to the inverse relationship between ΔT and R_T as stated in eq 2. Similar behavior is found for the other NH compositions. The change in the nature of the metallic shell (Au or Ag) has little impact on the ΔT values. On the contrary, it is found that a change in the core material from Fe₃O₄ to α -Fe₂O₃ leads to a significant increase of ΔT , which is mainly due to an increase in $C_{\text{abs,max}}$ (see Figure 3A). Figure 7 summarizes a large amount of simulations, and it should be useful, from a practical point of view, to optimize the design of NHs for photothermal applications. For instance, the optimum dimensions of a Fe₃O₄@Au NH that produce the largest ΔT when illuminated at a fixed incident wavelength of 800 nm are $R = 45 \text{ nm}$ and $S = 10 \text{ nm}$.

As mentioned above, all of the calculations were performed using water ($n_{\text{water}} = 1.33$) as the dielectric surrounding medium, which for biological applications is acceptable. However, it is important to note that, in more realistic situations, the presence of salts and the fact that protein corona are quickly formed around nanoparticles,⁶⁷ the refractive index of the environment may be higher than that of water. For instance, measured refractive indices of layers of some human proteins vary between 1.35 and 1.50.⁶⁸ Thus, it could be expected that the value of the effective refractive index n_{eff} experienced by a nanostructure immersed in a biological environment lies in the range $1.33 < n_{\text{eff}} < 1.50$, depending on its specific value on the particularities of a given biological media. As a consequence, this increase of n_{eff} in comparison with n_{water} should certainly produce a red-shift of the plasmon resonance as well as changes in the $C_{\text{abs,max}}$ values (see Figure S6). However, a thoroughly and more detailed study about this issue is beyond the scope of the current work and is the subject of current research in our group. Lastly, it is also important to consider the thermal conductivity of the surrounding medium when it is given by a biological environment. For instance, Foley et al. have measured the thermal conductivity κ at room temperature of bovine serum albumin and myoglobin films, reporting values of 0.23 and 0.19 $\text{W m}^{-1} \text{ K}^{-1}$, respectively.⁶⁹ Therefore, when the surrounding medium is changed from water ($\kappa_{\text{water}} = 0.6 \text{ W m}^{-1} \text{ K}^{-1}$) to a biological environment, larger ΔT values would be achieved by keeping the irradiance constant, by virtue of the inverse relationship between ΔT and κ (see eq 2). Alternatively, the same ΔT value could be achieved using a lower irradiance.

CONCLUSIONS

In this work, the optical properties of Fe₃O₄@Au, α -Fe₂O₃@Au, Fe₃O₄@Ag, and α -Fe₂O₃@Ag core-shell NHs have been studied by means of systematic electrostatics simulations based on the extended Mie theory. Due to the application of this kind of nanostructure in photothermal ablation therapies, focus has been made in investigating the variation of their absorption cross-section, C_{abs} , spectra with the core radius R and the shell thickness S . For all of the NH compositions studied, it has been found that the plasmon mode resonance wavelength, λ_{res} , red-shifts as the S/R ratio decreases, in agreement with previous results. In particular, NHs with Au shells present plasmon resonances more red-shifted than NHs with Ag shells of the same

size. More significant modifications in the absorption spectra have been observed when the core material was changed from Fe_3O_4 to $\alpha\text{-Fe}_2\text{O}_3$. In this case, a more pronounced red-shift of λ_{res} as well as an increase in the absorption peak intensity, $C_{\text{abs,max}}$ was found. These changes were attributed to the lower imaginary refractive index of $\alpha\text{-Fe}_2\text{O}_3$ in comparison to that of Fe_3O_4 . In addition, the $C_{\text{abs,max}}$ values obtained for different NH compositions, and within a broad range of R and S values, were employed to determine the temperature increase ΔT achieved at the surface of the NH when they are illuminated on resonance. In general, for NHs having a core material composed by $\alpha\text{-Fe}_2\text{O}_3$, larger ΔT values can be obtained than for NHs with Fe_3O_4 as the core material. In addition, diagrams that relate, for each NH composition, the core radius R , the shell thickness S , its resonance wavelength, and the temperature increase ΔT at its surface when the plasmon resonance mode is excited on resonance have been constructed. This set of diagrams summarizes key information that allows us to predict, for instance, the size and composition that a NH should have to produce the largest ΔT upon illumination at a certain wavelength. We believe the results presented in this work may be useful to optimize the design of magnetic-plasmonic core-shell NHs with potential photothermal applications.

■ ASSOCIATED CONTENT

■ Supporting Information

The Supporting Information is available free of charge on the ACS Publications website at DOI: 10.1021/acs.jpcc.5b11030.

Extinction, scattering, and absorption spectra of different sizes of $\text{Fe}_3\text{O}_4@Au$, $\text{Fe}_3\text{O}_4@Ag$, $\alpha\text{-Fe}_2\text{O}_3@Au$, and $\alpha\text{-Fe}_2\text{O}_3@Ag$ NHs dispersed in water (PDF)

■ AUTHOR INFORMATION

Corresponding Author

*(E.A.C.) E-mail: coronado@fcq.unc.edu.ar. Phone: +54-351-535-3866. Fax: +54-351-433-4180.

Notes

The authors declare no competing financial interest.

■ ACKNOWLEDGMENTS

We thank CONICET (PIP 112-201101-00430), FONCYT (PICT-2012-2286), and SECyT (UNC) for financial support.

■ REFERENCES

- (1) Zhao, P.; Li, N.; Astruc, D. State of the Art in Gold Nanoparticle Synthesis. *Coord. Chem. Rev.* **2013**, *257*, 638–665.
- (2) Ramasamy, K.; Malik, M. A.; Revaprasadu, N.; O'Brien, P. Routes to Nanostructured Inorganic Materials with Potential for Solar Energy Applications. *Chem. Mater.* **2013**, *25*, 3551–3569.
- (3) Roy, P.; Srivastava, S. K. Nanostructured Anode Materials for Lithium Ion Batteries. *J. Mater. Chem. A* **2015**, *3*, 2454–2484.
- (4) Xu, Y.; Chen, L.; Wang, X.; Yao, W.; Zhang, Q. Recent Advances in Noble Metal Based Composite Nanocatalysts: Colloidal Synthesis, Properties, and Catalytic Applications. *Nanoscale* **2015**, *7*, 10559–10583.
- (5) Baffou, G.; Quidant, R. Nanoplasmonics for Chemistry. *Chem. Soc. Rev.* **2014**, *43*, 3898–3907.
- (6) Wolfbeis, O. S. An Overview of Nanoparticles Commonly Used in Fluorescent Bioimaging. *Chem. Soc. Rev.* **2015**, *44*, 4743–4768.
- (7) Boulais, E.; Lachaine, R.; Hatef, A.; Meunier, M. Plasmonics for Pulsed-Laser Cell Nanosurgery: Fundamentals and Applications. *J. Photochem. Photobiol., C* **2013**, *17*, 26–49.
- (8) Kelly, K. L.; Coronado, E. A.; Zhao, L. L.; Schatz, G. C. The Optical Properties of Metal Nanoparticles: The Influence of Size, Shape, and Dielectric Environment. *J. Phys. Chem. B* **2003**, *107*, 668–677.
- (9) Encina, E. R.; Coronado, E. A. Resonance Conditions for Multipole Plasmon Excitations in Noble Metal Nanorods. *J. Phys. Chem. C* **2007**, *111*, 16796–16801.
- (10) Chen, H.; Shao, L.; Li, Q.; Wang, J. Gold Nanorods and their Plasmonic Properties. *Chem. Soc. Rev.* **2013**, *42*, 2679–2724.
- (11) Jiang, K.; Smith, D. A.; Pinchuk, A. Size-Dependent Photothermal Conversion Efficiencies of Plasmonically Heated Gold Nanoparticles. *J. Phys. Chem. C* **2013**, *117*, 27073–27080.
- (12) Govorov, A. O.; Zhang, W.; Skeini, T.; Richardson, H.; Lee, J.; Kotov, N. A. Gold Nanoparticle Ensembles as Heaters and Actuators: Melting and Collective Plasmon Resonances. *Nanoscale Res. Lett.* **2006**, *1*, 84–90.
- (13) Baffou, G.; Quidant, R.; Girard, C. Heat Generation in Plasmonic Nanostructures: Influence of Morphology. *Appl. Phys. Lett.* **2009**, *94*, 153109.
- (14) Baldwin, C. L.; Bigelow, N. W.; Masiello, D. J. Thermal Signatures of Plasmonic Fano Interferences: Toward the Achievement of Nanolocalized Temperature Manipulation. *J. Phys. Chem. Lett.* **2014**, *5*, 1347–1354.
- (15) Richardson, H. H.; Hickman, Z. N.; Govorov, A. O.; Thomas, A. C.; Zhang, W.; Kordes, M. E. Thermo-optical Properties of Gold Nanoparticles Embedded in Ice: Characterization of Heat Generation and Melting. *Nano Lett.* **2006**, *6*, 783–788.
- (16) Herzog, J. B.; Knight, M. W.; Natelson, D. Thermoplasmonics: Quantifying Plasmonic Heating in Single Nanowires. *Nano Lett.* **2014**, *14*, 499–503.
- (17) Baffou, G.; Quidant, R. Thermo-Plasmonics: Using Metallic Nanostructures as Nano-Sources of Heat. *Laser Photonics Rev.* **2013**, *7*, 171–187.
- (18) Baffou, G.; Quidant, R.; García de Abajo, F. J. Nanoscale Control of Optical Heating in Complex Plasmonic Systems. *ACS Nano* **2010**, *4*, 709–716.
- (19) Cornell, R. M.; Schwertmann, U. *The Iron Oxides: Structure, Properties, Reactions, Occurrence and Uses*; VCH: Weinheim, Germany, 2003.
- (20) Zhang, L.; Dong, W.-F.; Sun, H.-B. Multifunctional Superparamagnetic Iron Oxide Nanoparticles: Design, Synthesis and Biomedical Photonic Applications. *Nanoscale* **2013**, *5*, 7664–7684.
- (21) Wang, D.; Astruc, D. Fast-Growing Field of Magnetically Recyclable Nanocatalysts. *Chem. Rev.* **2014**, *114*, 6949–6985.
- (22) Wang, X.; Peng, K.; Hu, Y.; Zhang, F.; Hu, B.; Li, L.; Wang, M.; Meng, X.; Lee, S. Silicon/Hematite Core/Shell Nanowire Array Decorated with Gold Nanoparticles for Unbiased Solar Water Oxidation. *Nano Lett.* **2014**, *14*, 18–23.
- (23) Thimsen, E.; Le Formal, F.; Grätzel, M.; Warren, S. C. Influence of Plasmonic Au Nanoparticles on the Photoactivity of Fe_2O_3 Electrodes for Water Splitting. *Nano Lett.* **2011**, *11*, 35–43.
- (24) Manukyan, K. V.; Chen, Y.; Rouvimov, S.; Li, P.; Li, X.; Dong, S.; Liu, X.; Furdyna, J. K.; Orlov, A.; Bernstein, G. H.; Porod, W.; Roslyakov, S.; Mukasyan, A. Ultrasmall $\alpha\text{-Fe}_2\text{O}_3$ Superparamagnetic Nanoparticles with High Magnetization Prepared by Template-Assisted Combustion Process. *J. Phys. Chem. C* **2014**, *118*, 16264–16271.
- (25) Jiang, R.; Li, B.; Fang, C.; Wang, J. Metal/Semiconductor Hybrid Nanostructures for Plasmon-Enhanced Applications. *Adv. Mater.* **2014**, *26*, 5274–5309.
- (26) Qu, Y.; Duan, X. Progress, Challenge and Perspective of Heterogeneous Photocatalysts. *Chem. Soc. Rev.* **2013**, *42*, 2568–2580.
- (27) Cozzoli, P. D.; Pellegrino, T.; Manna, L. Synthesis, Properties and Perspectives of Hybrid Nanocrystal Structures. *Chem. Soc. Rev.* **2006**, *35*, 1195–1208.
- (28) Shi, W.; Zeng, H.; Sahoo, Y.; Ohulchanskyy, T. Y.; Ding, Y.; Wang, Z. L.; Swihart, M.; Prasad, P. N. A General Approach to Binary and Ternary Hybrid Nanocrystals. *Nano Lett.* **2006**, *6*, 875–881.
- (29) Sun, H.; He, J.; Wang, J.; Zhang, S.; Liu, C.; Sritharan, T.; Mhaisalkar, S.; Han, M.; Wang, D.; Chen, H. Investigating the Multiple

Roles of Polyvinylpyrrolidone for a General Methodology of Oxide Encapsulation. *J. Am. Chem. Soc.* **2013**, *135*, 9099–9110.

(30) Zhang, Y.; Ding, H.; Liu, Y.; Pan, S.; Luo, Y.; Li, G. Facile One-Step Synthesis of Plasmonic/Magnetic Core/Shell Nanostructures and their Multifunctionality. *J. Mater. Chem.* **2012**, *22*, 10779–10786.

(31) Chaudhuri, R. G.; Paria, S. Core/Shell Nanoparticles: Classes, Properties, Synthesis Mechanisms, Characterization, and Applications. *Chem. Rev.* **2012**, *112*, 2373–2433.

(32) Zhou, L.; Yuan, J.; Wei, Y. Core–Shell Structural Iron Oxide Hybrid Nanoparticles: from Controlled Synthesis to Biomedical Applications. *J. Mater. Chem.* **2011**, *21*, 2823–2840.

(33) Ma, Z.; Ha, H.; Tu, S.; Xue, J. Fabrication of Shape-Controlled Hematite Particles and Growth of Gold Nanoshells. *Colloids Surf., A* **2009**, *334*, 142–146.

(34) Lou, L.; Yu, K.; Zhang, Z.; Huang, R.; Wang, Y.; Zhu, Z. Facile Methods for Synthesis of Core–Shell Structured and Heterostructured Fe₃O₄@Au Nanocomposites. *Appl. Surf. Sci.* **2012**, *258*, 8521–8526.

(35) Mezni, A.; Balti, I.; Mlayah, A.; Jouini, N.; Smiri, L. S. Hybrid Au-Fe₃O₄ Nanoparticles: Plasmonic, Surface Enhanced Raman Scattering, and Phase Transition Properties. *J. Phys. Chem. C* **2013**, *117*, 16166–16174.

(36) Zhai, Y.; Zhai, J.; Wang, Y.; Guo, S.; Ren, W.; Dong, S. Fabrication of Iron Oxide Core/Gold Shell Submicrometer Spheres with Nanoscale Surface Roughness for Efficient Surface-Enhanced Raman Scattering. *J. Phys. Chem. C* **2009**, *113*, 7009–7014.

(37) Wang, L.; Luo, J.; Fan, Q.; Suzuki, M.; Suzuki, I. S.; Engelhard, M. H.; Lin, Y.; Kim, N.; Wang, J. Q.; Zhong, C. Monodispersed Core-Shell Fe₃O₄@Au Nanoparticles. *J. Phys. Chem. B* **2005**, *109*, 21593–21601.

(38) Lyon, J. L.; Fleming, D. A.; Stone, M. B.; Schiffer, P.; Williams, M. E. Synthesis of Fe Oxide Core/Au Shell Nanoparticles by Iterative Hydroxylamine Seeding. *Nano Lett.* **2004**, *4*, 719–723.

(39) Ke, F.; Wang, L.; Zhu, J. Multifunctional Au-Fe₃O₄@MOF Core-Shell Nanocomposite Catalysts with Controllable Reactivity and Magnetic Recyclability. *Nanoscale* **2015**, *7*, 1201–1208.

(40) Dong, W.; Li, Y.; Niu, D.; Ma, Z.; Gu, J.; Chen, Y.; Zhao, W.; Liu, X.; Liu, C.; Shi, J. Facile Synthesis of Monodisperse Superparamagnetic Fe₃O₄ Core@hybrid@Au Shell Nanocomposite for Bimodal Imaging and Photothermal Therapy. *Adv. Mater.* **2011**, *23*, 5392–5397.

(41) Bao, J.; Chen, W.; Liu, T.; Zhu, Y.; Jin, P.; Wang, L.; Liu, J.; Wei, J.; Li, Y. Bifunctional Au-Fe₃O₄ Nanoparticles for Protein Separation. *ACS Nano* **2007**, *4*, 293–298.

(42) Ji, X.; Shao, R.; Elliott, A. M.; Stafford, R. J.; Esparza-Coss, E.; Bankson, J. M.; Liang, G.; Luo, Z.; Park, K.; Markert, J. T.; Li, C. Bifunctional Gold Nanoshells with a Superparamagnetic Iron Oxide-Silica Core Suitable for Both MR Imaging and Photothermal Therapy. *J. Phys. Chem. C* **2007**, *111*, 6245–6251.

(43) Wang, D.; Zhu, X.; Lee, S.; Chan, H.; Li, H.; Kong, S. K.; Yu, J. C.; Cheng, C. H. K.; Wang, Y. J.; Leung, K. C. Folate-Conjugated Fe₃O₄@SiO₂@Gold Nanorods@Mesoporous SiO₂ Hybrid Nanomaterial: a Theranostic Agent for Magnetic Resonance Imaging and Photothermal Therapy. *J. Mater. Chem. B* **2013**, *1*, 2934–2942.

(44) Li, J.; Hu, Y.; Yang, J.; Wei, P.; Sun, W.; Shen, M.; Zhang, G.; Shi, X. Hyaluronic Acid-Modified Fe₃O₄@Au Core/Shell Nanostars for Multimodal Imaging and Photothermal Therapy of Tumors. *Biomaterials* **2015**, *38*, 10–21.

(45) Park, H.; Schadt, M. J.; Wang, L.; Lim, I. S.; Njoki, P. N.; Kim, S. H.; Jang, M.; Luo, J.; Zhong, C. Fabrication of Magnetic Core@Shell Fe Oxide@Au Nanoparticles for Interfacial Bioactivity and Bio-separation. *Langmuir* **2007**, *23*, 9050–9056.

(46) Wang, H.; Cao, G.; Gai, Z.; Hong, K.; Banerjee, P.; Zhou, S. Magnetic/NIR-Responsive Drug Carrier, Multicolor Cell Imaging, and Enhanced Photothermal-Therapy of Gold Capped Magnetite-Fluorescent Carbon Hybrid Nanoparticles. *Nanoscale* **2015**, *7*, 7885–7895.

(47) Wang, H.; Brandl, D. W.; Le, F.; Nordlander, P.; Halas, N. J. Nanorice: A Hybrid Plasmonic Nanostructure. *Nano Lett.* **2006**, *6*, 827–832.

(48) Brinson, B. E.; Lassiter, J. B.; Levin, C. S.; Bardhan, R.; Mirin, N.; Halas, N. J. Nanoshells Made Easy: Improving Au Layer Growth on Nanoparticle Surfaces. *Langmuir* **2008**, *24*, 14166–14171.

(49) Penninkhof, J. J.; Moroz, A.; van Blaaderen, A.; Polman, A. Optical Properties of Spherical and Oblate Spheroidal Gold Shell Colloids. *J. Phys. Chem. C* **2008**, *112*, 4146–4150.

(50) Hirsch, L. R.; Stafford, R. J.; Bankson, J. A.; Sershen, S. R.; Rivera, B.; Price, R. E.; Hazle, J. D.; Halas, N. H.; West, J. L. Nanoshell-Mediated Near-Infrared Thermal Therapy of Tumors Under Magnetic Resonance Guidance. *Proc. Natl. Acad. Sci. U. S. A.* **2003**, *100*, 13549–13554.

(51) Sotiriou, G. A.; Starsich, F.; Dasargyri, A.; Wurmig, M. C.; Krumeich, F.; Boss, A.; Leroux, J.; Pratsinis, S. E. Photothermal Killing of Cancer Cells by the Controlled Plasmonic Coupling of Silica-Coated Au/Fe₃O₄ Nanoaggregates. *Adv. Funct. Mater.* **2014**, *24*, 2818–2827.

(52) Abdulla-Al-Mamun, M.; Kusumoto, Y.; Zannat, T.; Horie, Y.; Manaka, H. Au-Ultrathin Functionalized Core–Shell (Fe₃O₄@Au) Monodispersed Nanocubes for a Combination of Magnetic/Plasmonic Photothermal Cancer Cell Killing. *RSC Adv.* **2013**, *3*, 7816–7827.

(53) Bardhan, R.; Lal, S.; Joshi, A.; Halas, N. J. Theranostic Nanoshells: From Probe Design to Imaging and Treatment of Cancer. *Acc. Chem. Res.* **2011**, *44*, 936–946.

(54) Brullot, W.; Valev, V. K.; Verbiest, T. Magnetic-Plasmonic Nanoparticles for the Life Sciences: Calculated Optical Properties of Hybrid Structures. *Nanomedicine* **2012**, *8*, 559–568.

(55) Chaffin, E.; Bhana, S.; O'Connor, R. T.; Huang, X.; Wang, Y. The Impact of Core Dielectric Properties on the Localized Surface Plasmonic Spectra of Gold-Coated Magnetic Core-Shell Nanoparticles. *J. Phys. Chem. B* **2014**, *118*, 14076–14084.

(56) Li, Q.; Zhang, W.; Zhao, D.; Qiu, M. Photothermal Enhancement in Core-Shell Structured Plasmonic Nanoparticles. *Plasmonics* **2014**, *9*, 623–630.

(57) Bohren, C. F.; Huffman, D. R. *Absorption and Scattering of Light by Small Particles*; Wiley-Interscience: New York, 1983.

(58) Palik, E. D. *Handbook of Optical Constant of Solids*; Academic Press: New York, 1985.

(59) Goossens, V.; Wielant, J.; Van Gils, S.; Finsy, R.; Terryn, H. Optical Properties of Thin Iron Oxide Films on Steel. *Surf. Interface Anal.* **2006**, *38*, 489–493.

(60) Ryde, N. P.; Matijević, E. Color Effects of Uniform Colloidal Particles of Different Morphologies Packed Into Films. *Appl. Opt.* **1994**, *33*, 7275–7281.

(61) Prodan, E.; Radloff, C.; Halas, N. J.; Nordlander, P. A Hybridization Model for the Plasmon Response of Complex Nanostructures. *Science* **2003**, *302*, 419–422.

(62) Prodan, E.; Nordlander, P. Plasmon Hybridization in Spherical Nanoparticles. *J. Chem. Phys.* **2004**, *120*, 5444–5454.

(63) Jain, P. K.; El-Sayed, M. A. Universal Scaling of Plasmon Coupling in Metal Nanostructures: Extension from Particle Pairs to Nanoshells. *Nano Lett.* **2007**, *7*, 2854–2858.

(64) Coronado, E. A.; Schatz, G. C. Surface Plasmon Broadening for Arbitrary Shape Nanoparticles: A Geometrical Probability Approach. *J. Chem. Phys.* **2003**, *119*, 3926–3934.

(65) Moroz, A. Electron Mean Free Path in a Spherical Shell Geometry. *J. Phys. Chem. C* **2008**, *112*, 10641–10652.

(66) Baffou, G.; Quidant, R.; Girard, C. Thermoplasmonics Modeling: A Green's Function Approach. *Phys. Rev. B: Condens. Matter Mater. Phys.* **2010**, *82*, 165424.

(67) Durán, N.; Silveira, C. P.; Durán, M.; Stéfani, D.; Martinez, T. Silver Nanoparticle Protein Corona and Toxicity: A Mini-Review. *J. Nanobiotechnol.* **2015**, *13*, 55.

(68) Vörös, J. The Density and Refractive Index of Adsorbing Protein Layers. *Biophys. J.* **2004**, *87*, 553–561.

(69) Foley, B. M.; Gorham, C. S.; Duda, J. C.; Cheaito, R.; Szejewski, C. J.; Constantin, C.; Kaehr, B.; Hopkins, P. E. Protein Thermal Conductivity Measured in the Solid State Reveals Anharmonic Interactions of Vibrations in a Fractal Structure. *J. Phys. Chem. Lett.* **2014**, *5*, 1077–1082.